Isotope Effects in 2D correlation infrared Spectra of Water: HEOM Analysis of Molecular Dynamics–Based Machine Learning Models

Kwanghee Park, Ryotaro Hoshino, and Yoshitaka Tanimura[a)]
Department of Chemistry, Graduate School of Science, Kyoto University, Kyoto 606-8502, Japan

(Dated: Last updated: 7 January 2026)

We model, simulate, and analyze the intramolecular modes of liquid H_2O and D_2O to elucidate how anharmonicity, energy relaxation, and vibrational dephasing interplay through anharmonic mode–mode coupling. Our analysis employs two-dimensional (2D) correlation spectra, a representative observable in nonlinear infrared vibrational spectroscopy. Accurate reproduction of these 2D spectral profiles requires not only a precise dynamical description of intramolecular vibrations but also an appropriate treatment of thermal environmental effects arising from strong interactions with surrounding molecules, which act as thermal baths. Capturing the essential features of the 2D spectra further demands a non-Markovian, non-perturbative, and nonlinear description of the interactions between intramolecular modes and their baths. To this end, we adopt a hierarchical equations of motion (HEOM) framework to compute the 2D spectra. By comparing the resulting spectra of H_2O and D_2O, we clarify the underlying mechanisms governing their complex energy and phase relaxation dynamics.

I. INTRODUCTION

Water molecules possess a simple molecular structure, yet the collective dynamics mediated by hydrogen bonding are remarkably complex, underpinning a wide range of chemical reactions and biological processes.[1] Isotope substitution provides a fundamental means of probing these intricate dynamics. Replacing H_2O with D_2O modifies zero-point energies and vibrational couplings, leading to measurable changes in spectral line shapes, coherence lifetimes, and reaction kinetics. Such isotope-dependent variations have been exploited to elucidate hydrogen-bonding networks,[2] clarify tunneling contributions,[3] and refine mechanistic models of aqueous reactions.[4] Ultrafast spectroscopic techniques, including X-ray free-electron laser experiments, offer direct access to the quantum properties of hydrogen-bonded liquids by probing femtosecond dynamics and isotope-dependent vibrational coupling.[5] In particular, nonlinear two-dimensional vibrational spectroscopy (2DVS)[6–16] has provided direct experimental evidence for isotope-dependent vibrational coupling and coherence lifetimes within hydrogen-bonded water networks.[17–21]

Recent theoretical studies have further shown that sparse hydroxyl solutes (e.g., HOD in liquid D_2O) serve as clean spectroscopic probes of the local hydrogen-bonding environment, owing to the OH stretching vibration's relative isolation from other modes.[22–29] Molecular dynamics (MD) simulations combined with empirical mappings between local electric fields and OH stretching frequencies have yielded valuable insights into IR, Raman, and 2D IR spectra.[30–36] However, discrepancies remain, particularly in spectral linewidths and echo peak-shift dynamics, highlighting the limitations of empirical frequency-field correlations and classical approximations in capturing the quantum nature of environmental interactions and spectral diffusion.[37–39]

Given the inherent difficulty of simulating nonlinear spectroscopy within a quantum MD framework, we have recently developed a suite of computational tools designed to overcome this challenge. These tools employ machine-learning (ML) techniques to parameterize a multimodal anharmonic Brownian (MAB) model directly from MD trajectories (`sbml4md`).[40–42] The resulting model provides a physically transparent platform for analyzing the roles of anharmonicity, energy relaxation, and vibrational dephasing as they interplay through anharmonic mode-mode coupling among intramolecular modes.

Capturing the essential features of the 2D spectra further demands a non-Markovian, non-perturbative, and nonlinear description of the interactions between intramolecular modes and their baths in both classical and quantum regimes. Therefore, in parallel with this research, our group developed a computational platform capable of rigorously treating (i) any two quantum inter- and intramolecular modes (`DHEOM-MLWS`),[43,44] (ii) any three classical inter- and intramolecular modes (`CHFPE-2DVS`),[45,46] and (iii) three quantum intramolecular modes (`HEOM-2DVS`),[47] thereby enabling the numerical computation of 2DVS. By combining these tools, we can model various solutions, including water, and obtain spectra such as 2D IR-Raman and 2D IR as needed. In this paper, we utilize this framework to model, simulate, and analyze the 2D correlation spectroscopy of H_2O and D_2O, thereby clarifying the underlying mechanisms governing their complex energy and phase relaxation dynamics.

This paper is organized as follows. Section II introduces our strategy, which combines MD and ML to parameterize the MAB model and compute 2D IR spectra via HEOM: MD → ML (`sbml4md`) → MAB model →

[a)]Author to whom correspondence should be addressed: tanimura.yoshitaka.5w@kyoto-u.jp

2D IR (`CHFPE-2DVS/HEOM-2DVS`). Section III presents the evaluated parameter values of the MAB model for H_2O and D_2O, along with the linear absorption and 2D correlation IR spectra calculated from them. Section IV is devoted to the summary.

II. MD SIMULATION, ML-BASED MAB MODELING, AND 2D IR VIA HEOM

Here, we briefly describe our complementary strategy for constructing data-driven models from atomic trajectories and for computing 2DVS by solving them within the HEOM framework. For clear illustration, we restrict the present discussion to the intramolecular modes of water, although the approach is in principle applicable to any solvent–solute system or to reaction centers within biomolecules.

A. MAB model

At the core of our approach is the MAB model. In this paper, we consider the three primary intramolecular modes of the water molecule: (1) anti-symmetric stretch, (1′) symmetric stretch, and (2) bending. These modes are described by dimensionless vibrational coordinates $\boldsymbol{q} = (q_1, q_{1'}, q_2)$. Each mode is independently coupled to the other optically inactive modes, which constitute a bath system represented by an ensemble of harmonic oscillators. The total Hamiltonian can then be expressed as[40–49]

$$\hat{H}_{tot} = \sum_s \left(\hat{H}_A^{(s)} + \hat{H}_I^{(s)} + \hat{H}_B^{(s)} + \hat{H}_C^{(s)})\right) + \tfrac{1}{2}\sum_{s\neq s'} \hat{U}_{ss'}(\hat{q}_s, \hat{q}_{s'}), \tag{1}$$

where

$$\hat{H}_A^{(s)} = \frac{\hat{p}_s^2}{2m_s} + \hat{U}_s(\hat{q}_s) \tag{2}$$

is the Hamiltonian for the sth mode ($s = 1, 1'$, and 2), with mass m_s, coordinate $\hat{q}_s$, and momentum $\hat{p}_s$; and

$$\hat{U}_s(\hat{q}_s) = \frac{1}{2} m_s \omega_s^2 \hat{q}_s^2 + \frac{1}{3!} g_{s^3} q_s^3 \tag{3}$$

is the anharmonic potential for the sth mode, described by the frequency ω_s and cubic anharmonicity g_{s^3}. The anhramonic coupling between the sth and s'th modes is given by

$$\hat{U}_{ss'}(\hat{q}_s, \hat{q}_{s'}) = g_{ss'}\hat{q}_s\hat{q}_{s'} + \frac{1}{6}\big(g_{s^2s'}\hat{q}_s^2\hat{q}_{s'} + g_{ss'^2}\hat{q}_s\hat{q}_{s'}^2\big), \tag{4}$$

where $g_{ss'}$ represents the second-order harmonicity, and $g_{s^2s'}$ and $g_{ss'^2}$ represent the third-order anharmonicity.

The bath Hamiltonian for the sth mode is expressed as[50,51]

$$\hat{H}_B^{(s)} = \sum_{j_s} \left(\frac{\hat{p}_{j_s}^2}{2m_{j_s}} + \frac{m_{j_s}\omega_{j_s}^2 \hat{x}_{j_s}^2}{2} \right), \tag{5}$$

where the momentum, coordinate, mass, and frequency of the j_sth bath oscillator are given by p_{j_s}, x_{j_s}, m_{j_s} and ω_{j_s}, respectively. The counter term is expressed as[52,53]

$$\hat{H}_C^{(s)} = \Lambda^{(s)} \hat{V}_s^2(\hat{q}_s) \tag{6}$$

with $\Lambda^{(s)} \equiv \sum_{j_s} \alpha_{j_s}^2 / 2m_{j_s}\omega_{j_s}^2$. The S-B interaction, defined as

$$H_{\mathrm{I}}^{(s)} = -V_s(\hat{q}_s) \textstyle\sum_{j_s} \alpha_{j_s} \hat{x}_{j_s}, \tag{7}$$

consists of linear-linear (LL)[54,55] and square-linear (SL) S-B interactions,[53,56,57] $V_s(\hat{q}_s) \equiv V_{\mathrm{LL}}^{(s)}\hat{q}_s + V_{\mathrm{SL}}^{(s)}\hat{q}_s^2/2$, with coupling strengths $V_{\mathrm{LL}}^{(s)}$, $V_{\mathrm{SL}}^{(s)}$, and α_{j_s}. For a vibrational mode with weak anharmonicity, the LL interaction leads to energy relaxation, while the SL interaction results in vibrational dephasing.[50,56]

The bath property is characterized by the SDF, defined as $J_s(\omega) \equiv \sum_{j_s} (\alpha_{j_s}^2 / 2m_{j_s}\omega_{j_s})\delta(\omega - \omega_{j_s})$.To employ the HEOM formalism, we consider the Drude SDF,

$$J_s(\omega) = \frac{m_s\zeta_s}{2\pi} \frac{\gamma_s^2 \omega}{\omega^2 + \gamma_s^2}. \tag{8}$$

The factor of the counter term is now given by

$$\Lambda^{(s)} = \frac{m_s\zeta_s\gamma_s}{2}. \tag{9}$$

B. Generation of MD Trajectories

The parameter variables of the MAB model are evaluated based on atomic trajectories generated by MD simulations. When using MD to obtain atomic trajectories for parameterizing the MAB model, the same precautions are required as when directly calculating multidimensional spectral profiles via MD simulations.[58–60] Several important considerations are summarized below.

System size. Because we aim to model fast intermolecular modes that originate from short-range intermolecular interactions, it is not necessary to perform large-scale simulations with many molecules. Thus, relatively small system sizes are sufficient, and even systems containing 200–300 molecules reproduce the qualitative behavior of liquid water.

Thermostat effects. Because 2DIR signals are highly sensitive to molecular dynamics, the use of thermostats such as the Nosé–Hoover or Langevin schemes can distort the 2D spectral profiles, particularly along the t_2 waiting-time axis. For accurate dynamical behavior, microcanonical (NVE) simulations are therefore preferred.

Force-field dependence. The 2DIR response strongly depends on the accuracy of the force field.

Differences in anharmonicity or structural fidelity lead to noticeable changes in the nonlinear response, even for nonpolar systems. Reliable force fields should therefore be validated against experimental structural data.

Long-range treatment of induced polarizability. The 2DIR profile is sensitive to the functional form of the induced polarizability. For many molecular systems, the Ewald summation is required to properly account for long-range dipole–dipole interactions, although the magnitude of the effect depends on the molecule.

Atomic trajectories for machine learning. For liquid water, a typical training trajectory has a total length of approximately 50 ps, with Cartesian coordinates of all atoms in all molecules saved every 0.1 fs. The required length of the underlying MD trajectory is evaluated from the linear absorption spectrum obtained directly from the simulation. Accurately reproducing the bending-mode peak requires a longer trajectory than that needed to capture the stretching-mode peak.

Notes for other molecular systems. Although the discussion above focuses on liquid water, similar considerations apply to other molecular systems. The required trajectory length, the sensitivity to thermostatting, and the importance of long-range electrostatics all depend on the characteristic timescales and interaction strengths of the system under study. For systems with slower structural relaxation or stronger intermolecular correlations, substantially longer MD trajectories may be necessary to achieve converged spectral features. Careful validation against experimental observables is therefore essential when extending the MAB parameterization to different molecular environments.

C. ML procedure (`sbml4md`)

The dynamical characteristics of the MAB model are defined by several key components: the vibrational potentials of the individual modes, the anharmonic mode–mode couplings, the functional forms of the linear and nonlinear interactions between the modes and the bath, and, critically, the SDF that governs the bath fluctuations. In our approach, these interaction forms are specified in advance, and their corresponding dynamical parameters are determined through ML optimization. The bath, treated as a continuum of degrees of freedom, is represented by a set of harmonic oscillators—typically numbering more than one thousandt—whose coupling constants are optimized to reproduce the MD results, from which the SDF parameters are subsequently inferred. With these elements in place, the algorithm developed by our group (`sbml4md`) proceeds as follows, illustrated here using the intramolecular vibrations of liquid water as a representative example.

1. Intramolecular Modes

By introducing the molecular system as a continuous function $J(\omega)$ described by Eq. (8), we have effectively considered a low-temperature heat bath with infinite specific heat, modeled by an infinite number of harmonic oscillators. In our description, the intramolecular modes (1), (1') and (2) are described in terms of the two O–H bond lengths and the H–O–H bond angle of the kth water molecule, defined as

$$r_1^k = \left|\mathbf{x}_{\mathrm{O}}^k - \mathbf{x}_{\mathrm{H}_1}^k\right|, \tag{10}$$

$$r_2^k = \left|\mathbf{x}_{\mathrm{O}}^k - \mathbf{x}_{\mathrm{H}_2}^k\right|, \tag{11}$$

and

$$\theta^k = \arccos\left(\frac{\left(\mathbf{x}_{\mathrm{O}}^k - \mathbf{x}_{\mathrm{H}_1}^k\right)\cdot\left(\mathbf{x}_{\mathrm{O}}^k - \mathbf{x}_{\mathrm{H}_2}^k\right)}{r_1 r_2}\right), \tag{12}$$

where $\mathbf{x}_{\mathrm{O}}$, $\mathbf{x}_{\mathrm{H}_1}$, and $\mathbf{x}_{\mathrm{H}_2}$are the positions of the oxygen, the 1st, and 2nd hydrogen atoms, respectively, describing the intramolecular motion of the kth molecule and r_1 and r_2 are the average length of r_1^k and r_2^k

The system coordinates for three intramolecular modes are expressed as

$$q_1^k = \frac{1}{2}\left(r_1^k - r_2^k\right), \tag{13}$$

$$q_{1'}^k = \frac{1}{2}\left(r_1^k + r_2^k - 2r_0\right), \tag{14}$$

$$q_2^k = \theta^k - \theta_0, \tag{15}$$

where the equilibrium values of r_0 and θ_0 are evaluated from the equilibrium distributions as $\langle r\rangle$ and $\langle\theta\rangle$. The system and S-B interaction, $H_{\mathrm{B}}^{(s)}$ and $H_{\mathrm{I}}^{(s)}$, are described with these system coordinates. The intramolecular mode-mode interaction, $U_{s,s'}(q_s, q_{s'})$, in the system Hamiltonian can be obtained by rewriting the intramolecular potentials appearing in Eqs.(3) and (4) in terms of Eqs. (13)-(15), respectively.

2. Bath oscilators

The degrees of freedom associated with the surrounding molecular motions, including the representative intermolecular vibrational mode, are treated as bath oscillators and are described by $H_{\mathrm{I}}^{(s)}$ and $H_{\mathrm{B}}^{(s)}$, given in Eqs. (5) and (7), respectively.

Within the ML framework, introducing a bath with infinitely many degrees of freedom is not feasible. Consequently, the bath coupled to the sth mode is represented by a system of N_s finite harmonic oscillators. The inverse of the interval $\Delta\omega_{N_s}$ between the eigenenergies of these oscillators determines the required sampling time of the trajectory, with longer times needed for smaller intervals. In practice, N_s is typically chosen between 1000 and 2000.

Under this prescription, the trajectory of the j_sth oscillator is given by

$$\tilde{x}_{j_s}(t) = A_{j_s}\sin(\omega_{j_s}t + \phi_{j_s}), \tag{16}$$

where ϕ_{j_s} is a random phase and A_{j_s} is a parameter learned within the ML framework. The amplitudes of the bath oscillators $\{A_{j_s}\}$ are utilized to determine the Drude SDF parameters (λ_s, γ_s), and $\{A_{j_s}\}$ are updated consistently with SDF throughout training. Because the SDF is defined through the anti-symmetric function of $\tilde{x}_{j_s}(t)$ as $\sum_{j_s}\langle\{\tilde{x}_{j_s}(t'), \tilde{x}_{j_s}(t)\}\rangle$, where $\{\cdot,\cdot\}$ denotes the Poisson bracket,[50] the SDF must be optimized with respect to $\langle\{V_s(t'), V_s(t)\}\rangle$ rather than the operator $V_s(\hat{q}_s) = V_{\rm LL}^{(s)}\hat{q}_s + V_{\rm SL}^{(s)}\hat{q}_s^2/2$. This indicates that $V_{\rm SL}^{(s)}$ cannot be determined independently of the Drude SDF strength ζ.

Because the overall scale of the SL coupling can be absorbed into the bath strength, there is a scale redundancy between the S-B coupling strength and $V_{\rm SL}^{(s)}$. To make this explicit, we factor out the SL coefficient and rewrite the interaction operator as $\hat{V}_s = V_{\rm SL}^{(s)}(\hat{q}_s^2 + \bar{V}_{\rm LL}^{(s)}\,\hat{q}_s$ wirh $\bar{V}_{\rm LL}^{(s)} \equiv V_{\rm LL}^{(s)}/V_{\rm SL}^{(s)}$.

We then optimize the coefficients through

$$c_{j_s}^k = \alpha_{j_s} V_{\rm LL}^{(s)} A_{j_s}, \tag{17}$$

which allows $\bar{V}_{\rm LL}^{(s)}$ to vary separately. We subsequently fix the gauge by applying a post-training normalization $V_{\rm SL}^{(s)} \to 1$ and absorb its magnitude into the bath-strength parameter as $\zeta_s \to \zeta_s\left(V_{\rm SL}^{(s)}\right)^2$.

In the SL-only calculations reported in this work, we set $V_{\rm LL}^{(s)} = 0$, so that $\bar{V}_{\rm LL}^{(s)} = 0$ and the coupling operator reduces to $\hat{V}_s = \hat{q}_s^2/2$ after normalization.

The bath parameters and S-B couplings are then encoded in the latent variables

$$\mathbf{z}_k = \left(\{c_{j_1}^k\}, \{c_{j_{1'}}^k\}, \{c_{j_2}^k\}\right), \tag{18}$$

where $\{c_{j_s}^k\}$ denotes the set of bath-coupling parameters.

3. ML optimaization

The trajectory of each molecule is then propagated using the MAB model:

$$\begin{aligned}\left(\tilde{\mathbf{q}}^k(t_0 + i\Delta t), \tilde{\mathbf{p}}^k(t_0 + i\Delta t)\right) &= \hat{L}(\Delta t; \mathbf{z}_k, \Sigma) \\ &\times (\tilde{\mathbf{q}}^k(t_0 + (i-1)\Delta t), \tilde{\mathbf{p}}^k(t_0 + (i-1)\Delta t)),\end{aligned} \tag{19}$$

where $\left(\tilde{\mathbf{q}}^k(t), \tilde{\mathbf{p}}^k(t)\right)$ denote the coordinates and momenta of the kth molecule. The operator $\hat{L}(\Delta t; \mathbf{z}_k, \Sigma)$ is the Liouvillian corresponding to Eqs. (1)–(7) with the discretized heat bath, and Σ denotes the set of system and bath parameters.

For each molecule, phase-space trajectories $(\mathbf{q}^k(t), \mathbf{p}^k(t))$ from MD are compared with MAB-predicted trajectories $(\bar{\mathbf{q}}^k(t), \bar{\mathbf{p}}^k(t))$. Parameters in Eqs.(3) and (4) and the SDF Eq. (8) are optimized to reproduce the reference MD data. We define the loss function as the Mean Squared Error (MSE) between the predicted and actual MD trajectories for the sth mode:

$$\mathrm{MSE}_{q_s} \equiv \tfrac{1}{N}\sum_{i=1}^{N}\left[\tilde{q}_s^k(t_i) - q_s^k(t_i)\right]^2. \tag{20}$$

Minimization of the above loss functions corresponds to the optimization of the learning model parameters. These include the anharmonicity of the potential energy surfaces, anharmonic mode-mode couplings, coupling strengths for LL and SL interactions, and the SDF parameters associated with each vibrational mode.

To optimize the MAB model parameters, we employ a generative ML scheme:

1. Read generated MD trajectories of water molecules from the input file.
2. Simulate corresponding trajectories with the MAB model under trial parameters.
3. Compute a loss function measuring deviation from MD references.
4. Backpropagate the loss to iteratively refine parameters.

D. CHFPE-2DVS

Once the optimized MAB variables are obtained, the spectrum is calculated using the HEOM framework. For Eqs. (1)–(9) with the Drude SDF [Eq. (8)], CHFPE-2DVS[45] and QHFPE-2DVS[47] have been established to treat three vibrational modes to simulate 2D correlation IR spectra.

In the CHFPE-2DVS, the terms associated with the Matsubara frequencies vanish, and the equations are expressed as follows[45,46,49]

$$\begin{aligned}\frac{\partial W^{(\boldsymbol{n})}(\boldsymbol{q},\boldsymbol{p};t)}{\partial t} &= (\hat{L}(\boldsymbol{q},\boldsymbol{p}) - \textstyle\sum_s n_s\gamma_s)W^{(\boldsymbol{n})}(\boldsymbol{q},\boldsymbol{p};t) \\ &+ \textstyle\sum_s \hat{\Phi}_s W^{(\boldsymbol{n}+\boldsymbol{e}_s)}(\boldsymbol{q},\boldsymbol{p};t) \\ &+ \textstyle\sum_s \hat{\Theta}_s W^{(\boldsymbol{n}-\boldsymbol{e}_s)}(\boldsymbol{q},\boldsymbol{p};t),\end{aligned} \tag{21}$$

where $W^{(\boldsymbol{n})}(\boldsymbol{q},\boldsymbol{p};t)$ is the Wigner distribution function (WDF) and the hierarchical elements are denoted as $\boldsymbol{n} = (n_1, n_2, n_3)$, where each n_s is a non-negative integer representing the sth mode, and $\boldsymbol{e}_s$ is the unit vector in the sth direction. Note that $W^{(\boldsymbol{n})}(\boldsymbol{q},\boldsymbol{p};t)$ has physical meaning only when $\boldsymbol{n} = (0,0,0)$; for all other values of $\boldsymbol{n}$, it serves as an auxiliary WDF that accounts for non-perturbative and non-Markovian S-B interactions.[50,51]

The classical Liouvillian $\hat{L}$ corresponding to the system Hamiltonian $H_{\rm sys}(\boldsymbol{q},\boldsymbol{p}) \equiv \sum_s H_A^{(s)} + \sum_{s<s'} U_{ss'}(\hat{q}_s, \hat{q}_{s'})$

is defined as

$$\hat{L}(\boldsymbol{q},\boldsymbol{p})W(\boldsymbol{q},\boldsymbol{p}) \equiv \{H_{\rm sys}(\boldsymbol{q},\boldsymbol{p}), W(\boldsymbol{q},\boldsymbol{p})\}_{\rm PB}, \tag{22}$$

where $\{\cdot,\cdot\}_{\rm PB}$ denotes the Poisson bracket, given by

$$\{A,B\}_{\rm PB} \equiv \sum_s \left(\frac{\partial A}{\partial q_s}\frac{\partial B}{\partial p_s} - \frac{\partial A}{\partial p_s}\frac{\partial B}{\partial q_s}\right) \tag{23}$$

for any functions A and B.

The operators $\hat{\Phi}_s$ and $\hat{\Theta}_s$ describe the energy exchange between the sth mode and its corresponding bath, and are defined as follows:[56,57]

$$\hat{\Phi}_s = \frac{\partial V_s(q_s)}{\partial q_s}\frac{\partial}{\partial p_s}, \tag{24}$$

and

$$\hat{\Theta}_s = \frac{m_s\zeta_s\gamma_s}{\beta}\frac{\partial V_s(q_s)}{\partial q_s}\frac{\partial}{\partial p_s} + \zeta_s\gamma_s p_s\frac{\partial V_s(q_s)}{\partial q_s}, \tag{25}$$

where ζ_s is the S-B coupling strength, γ_s is the inverse correlation time, and T is the temperature.

E. Linear absorption spectrum and 2D correlation spectra

For optical measurements in which the molecular system interacts with a laser field $E(t)$, the nonlinear components of the dipole moment are essential for describing 2D spectroscopy. Here we assume[43–46,49]

$$\hat{\mu} = \sum_s \mu^s \hat{q}_s + \frac{1}{2!}\sum_{s,s'} \mu^{ss'}\hat{q}_s\hat{q}_{s'}, \tag{26}$$

where μ_s and $\mu_{ss'}$ denote the linear and nonlinear elements

For the intramolecular three-mode vibration, the excitation frequency greatly exceeds thermal excitation, so the equilibrium state is taken as the ground state $|\mathbf{0}\rangle = |0_1, 0_{1'}, 0_2\rangle$. Applying the dipole operator $\hat{\mu}$ yields the excited state $|\mathbf{1}\rangle$, which contains single- and double-excitation components. A second application produces both returns to the ground state and higher excitations, collectively denoted as $|\mathbf{2}\rangle$.[47]

In the density operator representation, the first-order response function is[50,51]

$$R^{(1)}(t_1) = \left(\frac{i}{\hbar}\right)\mathrm{tr}\{\hat{\mu}\mathcal{G}(t_1)\hat{\mu}^\times\hat{\rho}^{\rm eq}\}, \tag{27}$$

where $\mathcal{G}(t)$ is the Green's function of the total Hamiltonian without a laser interaction, and $\hat{\rho}_{\rm eq}$ is the equilibrium state. whose Fourier transform gives the linear absorption spectrum $I(\omega) = \int_0^\infty dt R^{(1)}(t)\exp(\imath\omega t)$. The third-order response is

$$R^{(3)}(t_3,t_2,t_1) = \left(\frac{i}{\hbar}\right)^3\mathrm{tr}\{\hat{\mu}\mathcal{G}(t_3)\hat{\mu}^\times\mathcal{G}(t_2)\hat{\mu}^\times\mathcal{G}(t_1)\hat{\mu}^\times\hat{\rho}^{\rm eq}\}, \tag{28}$$

which expands into more than sixteen terms for three energy eigenstates. These include both population states such as $|\mathbf{1}\rangle\langle\mathbf{1}|$ and coherent states such as $|\mathbf{2}\rangle\langle\mathbf{1}|$.

In 2D correlation spectroscopy, coherent contributions are excluded.[61–63] Rephasing parts correspond to population states, while non-rephasing parts involve coherences. For density operators in the energy eigenbasis, separation is achieved by evaluating the specific Liouville pathways associated with excited-state populations and their conjugates, yielding the 2D correlation spectra. The detail of this procedure is explained in Refs, 47 and 51.

III. SIMULATION RESULTS AND DISCUSSIONS

A. MD simulation

Intermolecular interactions were modeled with the `mb-pol` potential,[33,34] a quantum-chemistry–based many-body framework that reproduces the properties of water across all phases with near–quantum-chemical accuracy. Training data were generated from molecular dynamics simulations performed with the `i-PI` driver,[64] which was coupled to an external force engine via the socket interface under classical conditions.

Simulations were carried out for liquid H_2O and D_2O systems, each containing 256 molecules in a cubic box of side length 19.7295 Å under periodic boundary conditions. Trajectories were propagated in the isothermal–isobaric (NPT) ensemble at $T = 298.15$ K and $P = 1$ atm, employing a Langevin thermostat ($\tau = 25$ fs) and an isotropic Langevin barostat ($\tau = 250$ fs). The equations of motion were integrated with a time step of 0.1 fs for a total of 500,000 steps (50 ps). Center-of-mass translational motion was removed to eliminate global drift associated with finite-precision integration. Cartesian coordinates were saved every 10 steps (1 fs), and thermodynamic quantities were recorded at each step. For D_2O, isotopic masses were explicitly assigned at initialization (O: 15.999 u, H: 1.008 u, D: 2.014 u).

B. ML parameterization

Based on the obtained MD trajectories, parameterization of the MAB model via ML was carried out following the procedure described in II C. In this work, we focus on the case in which $V_{\rm LL}$ is set to zero.

The thermal bath associated with each vibrational mode was represented by $N_s = 1500$ harmonic oscillators whose frequencies were defined as $\omega_{j_s} = j_s\Delta\omega$ with $\Delta\omega = 1$ ps^{-1} ≈ 5.31 cm^{-1}. This frequency grid spans up to 8000 cm^{-1}, thereby covering the overtone region of the OH stretching mode. The initial phases $\phi_{j_s}^k$ were randomly sampled from a uniform distribution over $[0, 2\pi)$ at each iteration step.

The MAB Hamiltonian [Eq. (1)] was propagated using a time step of 0.1 fs. The latent variables $\mathbf{z}_k$ were

TABLE I. Optimized parameters of the MAB model for isotopic water trained from `mb-pol` potential, incorporating the MAB model with the SL interaction: (1) anti-symmetric stretch, (1′) symmetric stretch, and (2) bending for H_2O and D_2O. Here, $\tilde{\zeta}_s$ denotes the normalized S-B coupling strength, and γ_s denotes the inverse correlation time of the bath fluctuations, $V_{\rm SL}^{(s)}$ denotes the SL interaction ($V_{\rm LL}^{(s)}=0$), and $\tilde{g}_{s^3}$ is the cubic anharmonicity for the s vibrational mode, respectively. We set the fundamental frequency to $\omega_0 = 4000$ cm^{-1}. The normalized parameters were defined as $\tilde{\zeta}_s \equiv (\omega_0/\omega_s)^2\zeta_s$, and $\tilde{g}_{s^3} \equiv (\omega_s/\omega_0)^3 g_{s^3}$. Nonlinear dipole elements are estimated from Ref. 45 and given by $\tilde{\mu}_{11'} = 1.2\times10^{-2}$, $\tilde{\mu}_{12}=0$, and $\tilde{\mu}_{1'2}=0$ with $\tilde{\mu}_{ss} \equiv (\omega_0/\omega_s)^2\mu_{ss}$.

	s	ω_s (cm^{-1})	γ_s/ω_0	$\tilde{\zeta}_s$	$V_{\rm SL}^{(s)}$	$\tilde{g}_{s^3}$
H_2O	1	3805	6.70×10^{-3}	6.09	1	-1.31×10^{-3}
	1′	3611	4.87×10^{-3}	3.45	1	-4.48×10^{-3}
	2	1623	5.36×10^{-3}	11.0	1	-2.59×10^{-2}
D_2O	1	2706	7.63×10^{-3}	3.43	1	-5.35×10^{-3}
	1′	2589	6.92×10^{-3}	4.90	1	-1.18×10^{-2}
	2	1234	5.41×10^{-3}	0.260	1	-5.18×10^{-2}

TABLE II. Optimized mode–mode coupling parameters of the MAB model for isotopic water trained from `mb-pol` potential, incorporating the MAB mode for (1) anti-symmetric stretch, (1′) symmetric stretch, and (2) bending modes. Here, we set $\tilde{g}_{s's} = g_{s's}(\omega_0/\omega_s)(\omega_0/\omega_{s'})$, $\tilde{g}_{s^2s'} = g_{s^2s'}(\omega_0/\omega_s)^2(\omega_0/\omega_{s'})$, and $\tilde{g}_{ss'^2} = g_{ss'^2}(\omega_0/\omega_s)(\omega_0/\omega_{s'})^2$.

	s − s′	$\tilde{g}_{ss'}$	$\tilde{g}_{s^2s'}$	$\tilde{g}_{ss'^2}$
H_2O	1 − 1′	4.06×10^{-1}	1.68×10^{-3}	6.11×10^{-4}
	1 − 2	1.03×10^{0}	4.91×10^{-3}	1.73×10^{-2}
	1′ − 2	1.14×10^{0}	5.22×10^{-3}	1.80×10^{-2}
D_2O	1 − 1′	8.32×10^{-1}	6.03×10^{-3}	1.37×10^{-3}
	1 − 2	1.86×10^{0}	1.12×10^{-2}	3.60×10^{-2}
	1′ − 2	1.93×10^{0}	1.34×10^{-2}	3.76×10^{-2}

initialized to zero, and both the system parameters and $\mathbf{z}_k$ were iteratively optimized. A minibatch size of 25 trajectories was used for each epoch, and the same set of trajectories was employed throughout the optimization. Iterations were continued until convergence of the potential parameters was achieved.

Model training was performed using Python 3.9.18 in conjunction with TensorFlow 2.15 and CUDA 12.2. All computations were executed on a system equipped with an Intel Core i9-13900H CPU and an NVIDIA GeForce RTX 4070 GPU.

The model parameters obtained for the MAB are summarized in Tables I and II.

C. CHFPE-2DVS calculations

The `CHFPE-2DVS` is time-integrated using the fourth-order Runge–Kutta method. Equation (21) is discretized using the compact finite-difference scheme on a non-uniform mesh.

For numerical integration, the hierarchy is truncated according to the condition $\delta_{\rm tot} > \Delta_{\boldsymbol{n}}/N$, where $N = \sum_s n_s$ and

$$\Delta_{\boldsymbol{n}} = \prod_s (n_s)^{-0.05}\,(k_B T m_s \zeta_s)^{n_s}\,. \tag{29}$$

By adjusting the number of hierarchical elements, the spectrum can be computed with the desired accuracy.

The entire integration routine is implemented in CUDA with the CUBLAS library and executed entirely on a GPU without memory transfer to the CPU. The source code was run on NVIDIA A100 (80 GB VRAM) GPU boards hosted on a workstation equipped with an Intel Xeon 6212U (24 cores).

1. Linear absorption spectra

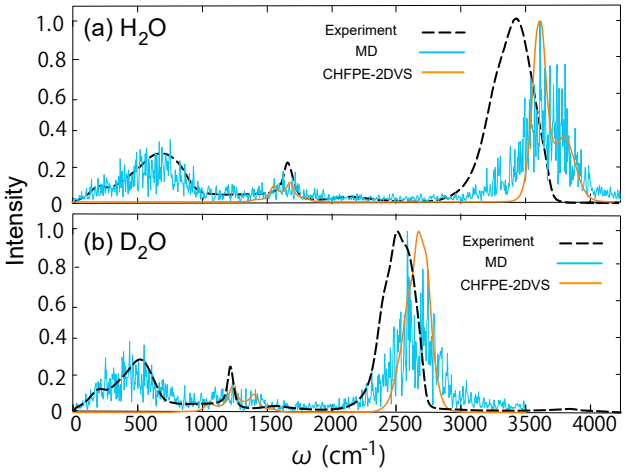

FIG. 1. Linear absorption spectra of (a) H_2O and (b) D_2O calculated using the three-mode MAB models with the parameter sets listed in Tables I and II. For comparison, each panel also includes results from MD simulations (blue lines) and experimental data (black dashed curves). Each spectrum is normalized to its maximum peak intensity. The H_2O experimental spectrum is reproduced with permission from Author, J. Mol. Struct. 1004, 146 (2011). Copyright (2011) Elsevier.[65] The D_2O experimental spectrum is reproduced from J. Chem. Phys. 131, 184505 (2009), with the permission of AIP Publishing.[66]

The linear absorption spectra of H_2O and D_2O obtained from the three-mode MAB model with the parameter sets listed in Tables I and II are shown in Fig. 1.

For reference, spectra from experimental results and those directly evaluated from MD trajectories are also presented. To obtain the MD-based spectrum, we used the total dipole moment $\boldsymbol{\mu}^{\rm tot}(t) = \boldsymbol{\mu}^{\rm perm}(t) + \boldsymbol{\mu}^{\rm ind}(t)$, evaluated at each sampling step. After removing the

time-averaged dipole $\langle \boldsymbol{\mu}^{\mathrm{tot}} \rangle$, we applied a real-valued FFT to each Cartesian component. The IR intensity was then computed as $I(\omega) \propto \omega^2 \sum_{\alpha=x,y,z} |\mu_\alpha^{\mathrm{tot}}(\omega)|^2$.

For both H_2O and D_2O, the stretching peaks of the high-frequency intramolecular modes appear blue-shifted relative to the experimental spectra, reflecting the absence of contributions from the zero-point oscillations in classical descriptions.[67]

Although the current MAB parameters were set from classical MD simulations, the force field (`mb-pol`) employed in those simulations was originally developed for quantum dynamical simulations of nuclei. Therefore, even if the MAB model variables are derived from classical trajectories, solving the resulting model quantum mechanically is expected to yield results equivalent to those obtained by performing the underlying MD quantum mechanically. This indicates that an MAB model can, in principle, be constructed from classical MD simulations when the underlying potential is designed to reproduce quantum-level accuracy. In addition to the blue-shifted peak positions, the CHFPE spectra exhibit narrower linewidths than the experimental spectra, reflecting the inability of classical dynamics to capture broadening mechanisms associated with quantum effects.

The MAB model provides a reasonable description of the stretch peak compared with the present results, aside from quantum effects. In contrast, its description of the bend peak deviates substantially from experimentally obtained spectra. Specifically, the bend peak shown in the present calculation results splits into two or three peaks. The stretch peak in the original MD spectrum is also attenuated, implying that the number of MD trajectories was likely insufficient to reproduce the bending peak. This inference is supported by comparison with previous flexible SPC/E and Ferguson results.[42] Taken together, these observations indicate that the present framework is a faithful approach that accurately reflects the quality and sampling depth of the underlying MD data.

2. 2D correlation IR spectra

Figures 2 and 3 show the 2D correlation spectra calculated at different t_2 periods using the MAB parameters for H_2O listed in Tables I and II. These results differ significantly from the 2D correlation IR spectrum calculated using CHFPE-2DVS with the MAB model variables chosen to reproduce the 2D IR-Raman simulation results for H_2O obtained with POLI2VS,[45] and they also differ substantially from the experimental results.

This difference reflects that, as shown in Fig. 2(a), the description of the model obtained through this optimization shows the two modes of stretching observed separately, and furthermore, that the bend peak is split. Indeed, the 2D profile in Figure 1 shows a total of four peaks, each appearing as a red–blue pair, observed around $\omega_1 = 3800\mathrm{cm}^{-1}$ for (1) anti-symmetric stretch and 3600 cm^{-1} for (1') symmetric stretch motions. Furthermore, in the bending-mode results shown in Fig. 3, two red–blue peak pairs are clearly observed, particularly for t_2 values of 100 fs or longer.

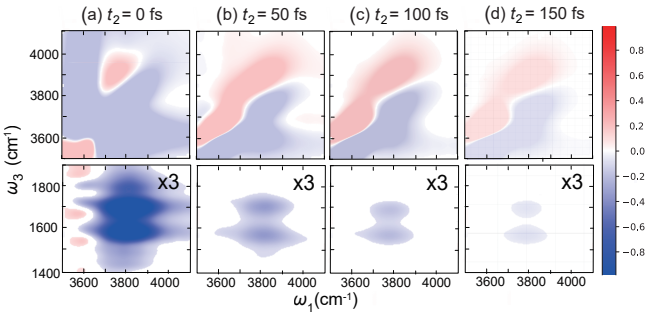

FIG. 2. The 2D correlation IR spectra of H_2O for the stretching modes (1) and (1') [upper panel] and the stretching (1, 1')–bending (2) motions [lower panels] at different t_2 periods were obtained using the parameter sets listed in Tables I and II. The spectral intensities were normalized to the maximum stretching amplitude. For improved visibility, the contour interval in the lower panels—where the peak intensities are weaker—was increased by a factor of three.

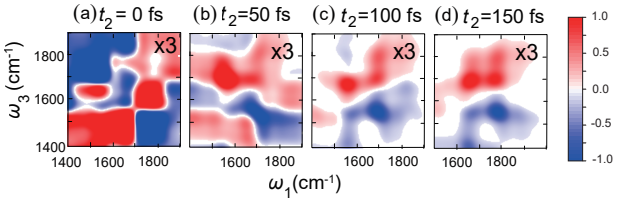

FIG. 3. The 2D correlation IR spectra of H_2O for the (2) bending motions were obtained using the parameter sets listed in Tables I and II. The spectral intensities were normalized to the maximum stretching amplitude. For emphasis, the peak intensity of the bending mode was multiplied by a factor of three relative to the intensity shown in Fig. 2.

In D_2O results in Figs. 4 and 5, where the excitation frequencies of both the stretching and bending modes are lower than in H_2O, differences in the overall spectral profile are expected. Nevertheless, the characteristic features of this modeled system that appear in the 1D spectra are also manifested in the 2DIR results. In particular, the stretching band broadens without splitting, whereas the bending band clearly splits into three distinct components.

Whether the clear discrepancies between the present spectrum and experimental observations—such as the peak splitting—can be resolved by performing quantum calculations with HEOM-2DVS for the same model remains to be verified in future work.

Excluding differences in spectral profiles arising from variations in the model, an examination of the contrast between H_2O and D_2O shows that, in D_2O, the narrower spacing between the stretch and bend modes leads to

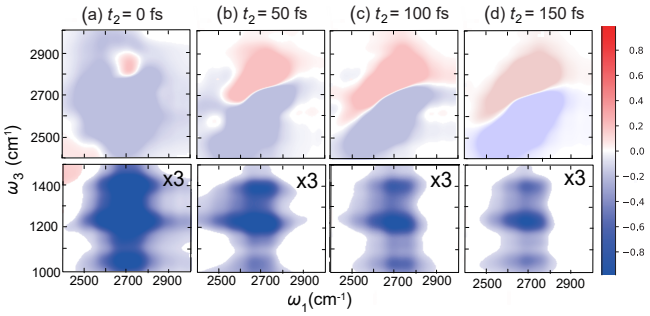

FIG. 4. The 2D correlation IR spectra of D_2O for the stretching modes (1) and (1') [upper panel] and the stretching (1, 1')–bending (2) motions [lower panels] at different t_2 periods. For emphasis, the contour interval in the lower panels was increased by a factor of three.

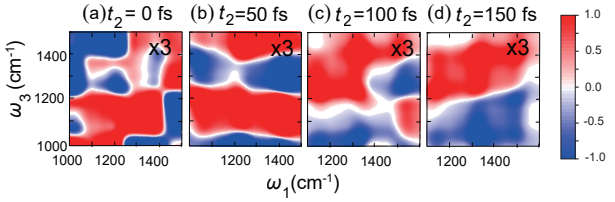

FIG. 5. The 2D correlation IR spectra of D_2O for the (2) bending motions were obtained using the parameter sets listed in Tables I and II. As the peak intensity was weaker than that in the upper panel of Fig. 4, the contour interval was tripled for emphasis.

stronger stretch–bend coupling. This enhanced coupling facilitates more efficient energy transfer and consequently results in a slower decay of the cross peak.

The water results suggest that the antisymmetric mode appears to be more strongly coupled to the bend than the stretch-bend crosspeak position. However, given that the bend peak is also split, determining whether this argument corresponds to actual water requires analysis—such as artificially altering coupling parameters—after improving the reproducibility of model experiments.

IV. CONCLUSION

In this study, we have demonstrated that the condensed-phase dynamics of intramolecular vibrations in H_2O and D_2O can be accurately captured by combining the `sbml4md` approach—which constructs MAB models directly from MD atomic orbitals—with the `CHFPE-2VS` method, which provides a rigorous numerical treatment of these models. The resulting linear absorption spectra and 2D correlated IR spectra reproduce key experimental features and reveal pronounced isotope-dependent differences in anharmonicity, intermolecular coupling, and both energy and vibrational relaxation. These distinctions, which are difficult to access or interpret using MD alone, underscore the essential role of properly incorporating bath effects in determining nonlinear spectroscopic responses.

The present results offer a unified mechanistic picture of vibrational dynamics in hydrogen-bonded liquids. By enabling systematic variation of physical conditions—such as the character of environmental fluctuations or the inclusion of quantum effects—beyond what is feasible in conventional MD, the proposed framework provides a powerful route for disentangling the fundamental factors that govern molecular motion in complex condensed-phase systems.

Because the `sbml4md` strategy employed here is intrinsically based on single MD trajectories, it can nevertheless be directly extended to solute molecules in solution, reaction centers in biomolecular environments, and other heterogeneous systems. By solving the quantum system using MAB model parameters determined from trajectories obtained via quantum MD and propagated with quantum HEOM, it becomes possible to incorporate quantum effects in a physically consistent manner. These directions represent promising avenues for future investigation.

ACKNOWLEDGMENTS

Y. T. was supported by JST (Grant No. CREST 1002405000170). K. P. acknowledges a fellowship supported by JST SPRING, the establishment of university fellowships toward the creation of science technology innovation (Grant No. JPMJSP2110).

AUTHOR DECLARATIONS

Conflict of Interest

The authors have no conflicts to disclose.

DATA AVAILABILITY

The data that support the findings of this study are available from the corresponding author upon reasonable request.

[1] I. Ohmine and S. Saito, "Water dynamics : fluctuation, relaxation, and chemical reactions in hydrogen bond network rearrangement," Accounts of Chemical Research **32**, 741–749 (1999).
[2] F. Paesani, "Water: Many-body potential for molecular simulations," Accounts of Chemical Research **52**, 273–281 (2019), review of molecular modeling approaches including isotope effects in hydrogen bonding.
[3] S. Cukierman, "Et tu, grotthuss! and other unfinished stories," Biochimica et Biophysica Acta (BBA) - Bioenergetics **1757**, 876–885 (2006), review of proton transfer and isotope effects in hydrogen-bonded networks.

[4]A. Kohen and H.-H. Limbach, Isotope Effects in Chemistry and Biology (CRC Press, 2010) extensive reference on kinetic isotope effects and their role in chemical mechanisms.

[5]R. Guillemin et al., "Isotope effects in dynamics of water isotopologues induced by core ionization at an x-ray free-electron laser," Struct. Dyn. **10**, 054302 (2023).

[6]M. Cowan, B. Bruner, N. Huse, J. Dwyer, B. Chugh, E. Nibbering, T. Elsaesser, and R. Miller, "Ultrafast memory loss and energy redistribution in the hydrogen bond network of liquid H_2O," NATURE **434**, 199–202 (2005).

[7]N. Huse, S. Ashihara, E. Nibbering, and T. Elsaesser, "Ultrafast vibrational relaxation of O-H bending and librational excitations in liquid H_2O," CHEMICAL PHYSICS LETTERS **404**, 389–393 (2005).

[8]D. Kraemer, M. L. Cowan, A. Paarmann, N. Huse, E. T. J. Nibbering, T. Elsaesser, and R. J. D. Miller, "Temperature dependence of the two-dimensional infrared spectrum of liquid H_2O," Proceedings of the National Academy of Sciences **105**, 437–442 (2008).

[9]A. Tokmakoff, "Two-dimensional infrared spectroscopy of water," J. Chem. Phys. **116**, 5563–5579 (2002).

[10]C. Fecko, J. Eaves, J. Loparo, A. Tokmakoff, and P. Geissler, "Ultrafast hydrogen-bond dynamics in the infrared spectroscopy of water," SCIENCE **301**, 1698–1702 (2003).

[11]J. D. Eaves, A. Tokmakoff, and P. L. Geissler, "Electric field fluctuations drive vibrational dephasing in water," The Journal of Physical Chemistry A **109**, 9424–9436 (2005), pMID: 16866391.

[12]M. Thämer, L. D. Marco, K. Ramasesha, A. Mandal, and A. Tokmakoff, "Ultrafast 2d IR spectroscopy of the excess proton in liquid water," Science **350**, 78–82 (2015).

[13]L. De Marco, J. A. Fournier, M. Thämer, W. Carpenter, and A. Tokmakoff, "Anharmonic exciton dynamics and energy dissipation in liquid water from two-dimensional infrared spectroscopy," The Journal of Chemical Physics **145**, 094501 (2016), https://aip.scitation.org/doi/pdf/10.1063/1.4961752.

[14]N. H. C. Lewis, B. Dereka, Y. Zhang, E. J. Maginn, and A. Tokmakoff, "From networked to isolated: Observing water hydrogen bonds in concentrated electrolytes with two-dimensional infrared spectroscopy," The Journal of Physical Chemistry B **126**, 5305–5319 (2022), pMID: 35829623, https://doi.org/10.1021/acs.jpcb.2c03341.

[15]A. A. Bakulin, C. Liang, T. la Cour Jansen, D. A. Wiersma, H. J. Bakker, and M. S. Pshenichnikov, "Hydrophobic solvation: A 2d ir spectroscopic inquest," Accounts of Chemical Research **42**, 1229–1238 (2009), https://doi.org/10.1021/ar9000247.

[16]P. Hamm and M. Zanni, Concepts and Methods of 2D Infrared Spectroscopy (Cambridge University Press, 2011) comprehensive reference on experimental 2D IR methods applied to water and isotope effects.

[17]T. Yagasaki and S. Saito, "Fluctuations and relaxation dynamics of liquid water revealed by linear and nonlinear spectroscopy," Annual Review of Physical Chemistry **64**, 55–75 (2013), https://doi.org/10.1146/annurev-physchem-040412-110150.

[18]T. Yagasaki and S. Saito, "Ultrafast intermolecular dynamics of liquid water: A theoretical study on two-dimensional infrared spectroscopy," The Journal of Chemical Physics **128**, 154521 (2008), https://doi.org/10.1063/1.2903470.

[19]B. Auer, R. Kumar, J. R. Schmidt, and J. L. Skinner, "Hydrogen bonding and raman, ir, and 2d-ir spectroscopy of dilute hod in liquid d¡sub¿2¡/sub¿o," Proceedings of the National Academy of Sciences **104**, 14215–14220 (2007).

[20]T. l. C. Jansen, B. M. Auer, M. Yang, and J. L. Skinner, "Two-dimensional infrared spectroscopy and ultrafast anisotropy decay of water," The Journal of Chemical Physics **132**, 224503 (2010).

[21]T. l. C. Jansen, S. Saito, J. Jeon, and M. Cho, "Theory of coherent two-dimensional vibrational spectroscopy," The Journal of Chemical Physics **150**, 100901 (2019), https://doi.org/10.1063/1.5083966.

[22]R. Rey, K. B. Møller, and J. T. Hynes, "Hydrogen bond dynamics in water and ultrafast infrared spectroscopy," The Journal of Physical Chemistry A **106**, 11993–11996 (2002).

[23]C. P. Lawrence and J. L. Skinner, "Vibrational spectroscopy of hod in liquid d2o. I. vibrational energy relaxation," The Journal of Chemical Physics **117**, 5827–5838 (2002).

[24]C. P. Lawrence and J. L. Skinner, "Vibrational spectroscopy of hod in liquid d2o. II. infrared line shapes and vibrational stokes shift," The Journal of Chemical Physics **117**, 8847–8854 (2002).

[25]C. P. Lawrence and J. L. Skinner, "Vibrational spectroscopy of hod in liquid d2o. III. spectral diffusion, and hydrogen-bonding and rotational dynamics," The Journal of Chemical Physics **118**, 264–272 (2003).

[26]A. Piryatinski, C. P. Lawrence, and J. L. Skinner, "Vibrational spectroscopy of hod in liquid d2o. iv. infrared two-pulse photon echoes," The Journal of Chemical Physics **118**, 9664–9671 (2003).

[27]A. Piryatinski, C. P. Lawrence, and J. L. Skinner, "Vibrational spectroscopy of HOD in liquid D_2O. v. infrared three-pulse photon echoes," The Journal of Chemical Physics **118**, 9672–9679 (2003), https://doi.org/10.1063/1.1569474.

[28]S. A. Corcelli, C. P. Lawrence, and J. L. Skinner, "Combined electronic structure/molecular dynamics approach for ultrafast infrared spectroscopy of dilute hod in liquid h2o and d2o," The Journal of Chemical Physics **120**, 8107–8117 (2004).

[29]S. A. Corcelli and J. L. Skinner, "Infrared and raman line shapes of dilute hod in liquid h2o and d2o from 10 to 90°c," The Journal of Physical Chemistry A **109**, 6154–6165 (2005), pMID: 16833955.

[30]J. Liu, W. H. Miller, G. S. Fanourgakis, S. S. Xantheas, S. Imoto, and S. Saito, "Insights in quantum dynamical effects in the infrared spectroscopy of liquid water from a semiclassical study with an ab initio-based flexible and polarizable force field," The Journal of Chemical Physics **135**, 244503 (2011), https://doi.org/10.1063/1.3670960.

[31]S. Imoto, S. S. Xantheas, and S. Saito, "Ultrafast dynamics of liquid water: Frequency fluctuations of the OH stretch and the HOH bend," The Journal of Chemical Physics **139**, 044503 (2013), https://doi.org/10.1063/1.4813071.

[32]S. Imoto, S. S. Xantheas, and S. Saito, "Ultrafast dynamics of liquid water: Energy relaxation and transfer processes of the OH stretch and the HOH bend," The Journal of Physical Chemistry B **119**, 11068–11078 (2015), pMID: 26042611, https://doi.org/10.1021/acs.jpcb.5b02589.

[33]V. Babin, C. Leforestier, and F. Paesani, "Development of a "first principles" water potential with flexible monomers: Dimer potential energy surface, VRT spectrum, and second virial coefficient," Journal of Chemical Theory and Computation **9**, 5395–5403 (2013), pMID: 26592277.

[34]V. Babin, G. R. Medders, and F. Paesani, "Development of a "first principles" water potential with flexible monomers. II: Trimer potential energy surface, third virial coefficient, and small clusters," Journal of Chemical Theory and Computation **10**, 1599–1607 (2014), pMID: 26580372.

[35]M. Rossi, H. Liu, F. Paesani, J. Bowman, and M. Ceriotti, "Communication: On the consistency of approximate quantum dynamics simulation methods for vibrational spectra in the condensed phase," The Journal of Chemical Physics **141**, 181101 (2014), https://doi.org/10.1063/1.4901214.

[36]G. R. Medders, V. Babin, and F. Paesani, "Development of a "first-principles" water potential with flexible monomers. iii. liquid phase properties," Journal of Chemical Theory and Computation **10**, 2906–2910 (2014), pMID: 26588266, https://doi.org/10.1021/ct5004115.

[37]K. M. Hunter, F. A. Shakib, and F. Paesani, "Disentangling coupling effects in the infrared spectra of liquid water," The Journal of Physical Chemistry B **122**, 10754–10761 (2018), pMID: 30403350, https://doi.org/10.1021/acs.jpcb.8b09910.

[38]X. Liu and J. Liu, "Critical role of quantum dynamical effects in the Raman spectroscopy of liq-

uid water," Molecular Physics **116**, 755–779 (2018), https://doi.org/10.1080/00268976.2018.1434907.

[39]G. Trenins, M. J. Willatt, and S. C. Althorpe, "Path-integral dynamics of water using curvilinear centroids," The Journal of Chemical Physics **151**, 054109 (2019), https://doi.org/10.1063/1.5100587.

[40]S. Ueno and Y. Tanimura, "Modeling intermolecular and intramolecular modes of liquid water using multiple heat baths: Machine learning approach," Journal of Chemical Theory and Computation **16**, 2099–2108 (2020).

[41]K. Park, J.-Y. Jo, and Y. Tanimura, "System–bath modeling in vibrational spectroscopy via molecular dynamics: A machine learning framework for hierarchical equations of motion (heom)," The Journal of Chemical Physics **163**, 214104 (2025).

[42]K. Park, S. Ueno, and Y. Tanimura, "sbml4md: A computational platform for system-bath modeling via molecular dynamics powered by machine learning," The Journal of Chemical Physics **16x**, xxxx (2026).

[43]H. Takahashi and Y. Tanimura, "Discretized hierarchal equations of motion in mixed Liouville–Wigner space for two-dimensional vibrational spectroscopies of water," The Journal of Chemical Physics **158**, 044115 (2023), arXiv:2302.09799.

[44]H. Takahashi and Y. Tanimura, "Simulating two-dimensional correlation spectroscopies with third-order infrared and fifth-order infrared–Raman processes of liquid water," The Journal of Chemical Physics **158**, 124108 (2023), arXiv:2302.09760.

[45]R. Hoshino and Y. Tanimura, "Analysis of intramolecular modes of liquid water in two-dimensional spectroscopy: A classical hierarchical equations of motion approach," The Journal of Chemical Physics **162**, 044105 (2025), https://pubs.aip.org/aip/jcp/article-pdf/doi/10.1063/5.0245564/20360227/044105_1_5.0245564.pdf.

[46]R. Hoshino and Y. Tanimura, "A multimode classical hierarchical Fokker–Planck equations approach to molecular vibrations: Simulating two-dimensional spectra," The Journal of Chemical Physics **163**, 172501 (2025).

[47]R. Hoshino and Y. Tanimura, "HEOM-based numerical framework for quantum simulation of two-dimensional vibrational spectra in molecular liquids," The Journal of Chemical Physics **16x**, xxxx (2026).

[48]T. Ikeda, H. Ito, and Y. Tanimura, "Analysis of 2D THz-Raman spectroscopy using a non-Markovian Brownian oscillator model with nonlinear system-bath interactions," The Journal of Chemical Physics **142**, 212421 (2015).

[49]H. Ito and Y. Tanimura, "Simulating two-dimensional infrared-Raman and Raman spectroscopies for intermolecular and intramolecular modes of liquid water," The Journal of Chemical Physics **144**, 074201 (2016).

[50]Y. Tanimura, "Stochastic Liouville, Langevin, Fokker-Planck, and master equation qpproaches to quantum dissipative systems," Journal of the Physical Society of Japan **75**, 082001 (2006).

[51]Y. Tanimura, "Numerically "exact" approach to open quantum dynamics: The hierarchical equations of motion (HEOM)," The Journal of Chemical Physics **153**, 020901 (2020).

[52]Y. Tanimura and P. G. Wolynes, "Quantum and classical Fokker-Planck equations for a Gaussian-Markovian noise bath," Phys. Rev. A **43**, 4131–4142 (1991).

[53]K. Okumura and Y. Tanimura, "Two-time correlation functions of a harmonic system nonbilinearly coupled to a heat bath: Spontaneous Raman spectroscopy," Phys. Rev. E **56**, 2747–2750 (1997).

[54]Y. Tanimura and S. Mukamel, "Two-dimensional femtosecond vibrational spectroscopy of liquids," The Journal of Chemical Physics **99**, 9496–9511 (1993).

[55]Y. Tanimura, "Fifth-order two-dimensional vibrational spectroscopy of a Morse potential system in condensed phases," Chemical Physics **233**, 217–229 (1998).

[56]Y. Tanimura and T. Steffen, "Two-dimensional spectroscopy for harmonic vibrational modes with nonlinear system-bath interactions.ii. Gaussian-Markovian case," Journal of the Physical Society of Japan **69**, 4095–4106 (2000).

[57]T. Kato and Y. Tanimura, "Two-dimensional Raman and infrared vibrational spectroscopy for a harmonic oscillator system nonlinearly coupled with a colored noise bath," The Journal of Chemical Physics **120**, 260–271 (2004).

[58]H. Ito, J.-Y. Jo, and Y. Tanimura, "Notes on simulating two-dimensional Raman and terahertz-Raman signals with a full molecular dynamics simulation approach," Structural Dynamics **2**, 054102 (2015).

[59]T. Hasegawa and Y. Tanimura, "Nonequilibrium molecular dynamics simulations with a backward-forward trajectories sampling for multidimensional infrared spectroscopy of molecular vibrational modes," The Journal of Chemical Physics **128**, 064511 (2008).

[60]T. Hasegawa and Y. Tanimura, "A polarizable water model for intramolecular and intermolecular vibrational spectroscopies," The Journal of Physical Chemistry B **115**, 5545–5553 (2011).

[61]J. D. Hybl, A. Albrecht Ferro, and D. M. Jonas, "Two-dimensional fourier transform electronic spectroscopy," The Journal of Chemical Physics **115**, 6606–6622 (2001), https://doi.org/10.1063/1.1398579.

[62]N.-H. Ge, M. T. Zanni, and R. M. Hochstrasser, "Effects of vibrational frequency correlations on two-dimensional infrared spectra†," Journal of Physical Chemistry A **106**, 962–972 (2002).

[63]M. Khalil, N. Demirdöven, and A. Tokmakoff, "Obtaining absorptive line shapes in two-dimensional infrared vibrational correlation spectra," Phys. Rev. Lett. **90**, 047401 (2003).

[64]Y. Litman, V. Kapil, Y. M. Y. Feldman, D. Tisi, T. Begušić, K. Fidanyan, G. Fraux, J. Higer, M. Kellner, T. E. Li, E. S. Pós, E. Stocco, G. Trenins, B. Hirshberg, M. Rossi, and M. Ceriotti, "i-pi 3.0: a flexible and efficient framework for advanced atomistic simulations," J. Chem. Phys. **161**, 062505 (2024).

[65]Y. Maréchal, "The molecular structure of liquid water delivered by absorption spectroscopy in the whole IR region completed with thermodynamics data," Journal of Molecular Structure **1004**, 146–155 (2011).

[66]J.-J. Max and C. Chapados, "Isotope effects in liquid water by infrared spectroscopy. iii. h2o and d2o spectra from 6000 cm-1," The Journal of Chemical Physics **131**, 184505 (2009).

[67]A. Sakurai and Y. Tanimura, "Does $\hbar$ play a role in multidimensional spectroscopy? reduced hierarchy equations of motion approach to molecular vibrations," The Journal of Physical Chemistry A **115**, 4009–4022 (2011).